A momentum-space theory for topological magnons in 2D ferromagnetic skyrmion lattices

Doried Ghader*[1] and Bilal Jabakhanji[1]

[1] College of Engineering and Technology, American University of the Middle East, Egaila 54200, Kuwait

*doried.ghader@aum.edu.kw

Abstract

Magnon dynamics in skyrmion lattices have garnered significant interest due to their potential applications in topological magnonics. Existing theories often follow a single-momentum approach, assuming significant Dzyaloshinskii-Moriya Interaction (DMI) to minimize the skyrmion's dimensions, which can lead to oversimplification in describing magnon behavior. This study introduces a multi-momentum operator theory for magnons in large 2D skyrmions, where each skyrmion encompasses several thousand spins. The proposed theory fully transforms the magnon Hamiltonian into momentum space, incorporating off-diagonal terms to capture umklapp scattering caused by the skyrmion wave vectors. Our results reveal deviations from single-momentum theories, demonstrating that flat bands are not universal features of the skyrmionic magnon spectrum. Additionally, we find that manipulating the skyrmion size with an external magnetic field induces multiple topological phase transitions. At high magnetic fields, the low-energy magnon spectrum becomes densely packed and entirely topological, resembling a topological band continuum.

Introduction

Skyrmion lattices are compelling platforms for probing unconventional magnon dynamics[1–5], holding significant potential for advancements in topological magnonics[6]. Theories[1,7–10] suggest that the topological winding of the skyrmion generates a fictitious magnetic field that acts upon magnons, thereby influencing their dynamical behavior. This emergent interaction between magnons and the underlying spin texture leads to topological magnon bands with finite Berry curvatures and nonzero Chern numbers. Recent experiments[4,11] supported the theoretical predictions, presenting solid evidence of topological magnon bands and thermal magnon Hall effect in skyrmion lattices.

Operator-based theories on skyrmionic magnons[3,7–9,12–14] commonly treat the skyrmion lattice as a "cluster" (or a collection of sublattices), where each spin in the unit cell (representing a single skyrmion) introduces a sublattice magnon operator. In this framework, a large Dzyaloshinskii-Moriya Interaction (DMI) is often assumed to minimize the dimensions of the skyrmion. By

maintaining a real-space cluster description, the resulting Hamiltonian becomes a single-momentum operator that forces magnons to travel with uniform momenta, potentially oversimplifying the complex dynamics of magnons in skyrmion lattices.

In most materials, the DMI stabilizing the skyrmion lattice is typically weak, leading to skyrmions encompassing several thousand spins. This large scale renders the cluster approach less practical for studying magnons and potentially insufficient for fully capturing the effects of the skyrmion spin texture on magnon dynamics. Large skyrmions effectively form a continuum that can be reconstructed via a set of characteristic wave vectors. The skyrmion wave vectors are pivotal in shaping the magnon dynamics, as they lead to umklapp scattering events that alter the magnon's momentum. Capturing this complex interaction landscape and its effect on magnon dynamics is beyond the reach of single-momentum Hamiltonians, necessitating a theory that encodes the skyrmion wave vectors into the magnons' operators.

This work introduces a momentum-space theory to explore magnon dynamics in large 2D ferromagnetic skyrmions. Employing Fourier-space techniques, we construct a momentum-space representation of the skyrmion lattice, associating magnon operators with sites defined by the skyrmion lattice's wave vectors. Utilizing these operators, we derive a multi-momentum magnon Hamiltonian, with diagonal and off-diagonal terms capturing ordinary and umklapp magnon scatterings, respectively. The magnon spectra obtained from this approach underscore the crucial role of skyrmion size, determined by the magnetic field for a given DMI, in shaping magnon dynamics. The magnetic field compacts the magnon spectrum, leaving small gaps between adjacent bands that enable valid definitions of the Berry curvatures and Chern numbers. The number of topological bands increases with higher magnetic fields, while flat bands are rarely observed, even at a minimal magnetic field. This suggests that the magnetic field induces multiple topological phase transitions, rather than a single transition at a critical magnetic field value[9]. Notably, at the maximal magnetic field, flat bands are absent, and the entire low-energy magnon spectrum becomes topological and densely packed, resembling a continuum of topological bands.

Theory

This section concisely presents our theory, while detailed derivations are provided in the Supplementary Notes. We start by considering a 2D triangular lattice of spins on the xy-plane, described by the real-space Hamiltonian:

$$\mathcal{H} = -J \sum_{i,j} \boldsymbol{S}_i . \boldsymbol{S}_j - \sum_{i,j} \boldsymbol{D}_{ij} . \boldsymbol{S}_i \times \boldsymbol{S}_j - B \sum_i S_i^z$$

(1)

In Equation 1, $\boldsymbol{S}_i$ denotes the spin operator at site i. The terms in order represent the nearest neighbor (NN) ferromagnetic exchange, chiral NN DMI[15,16] compatible with interfacial inversion symmetry breaking[17,18], and Zeeman coupling due to an external magnetic ($\boldsymbol{B}$) along the z-axis. The DMI vectors are given by $\boldsymbol{D}_{ij} = D\hat{\boldsymbol{z}} \times \hat{\boldsymbol{r}}_{ij}$, where $\hat{\boldsymbol{z}}$ and $\hat{\boldsymbol{r}}_{ij}$ are unit vectors along the z-axis and the NN bond, respectively. The coefficients J and D quantify the strengths of the exchange and DMI, respectively.

For suitable values of B, the classical ground state of the Hamiltonian forms a ferromagnetic skyrmion lattice[3,4,7–9,19–23], which we simulate using the stochastic Landau-Lifshitz-Gilbert equations (sLLG) within the Vampire software[24]. We achieved large skyrmions by assuming a weak DMI ($D = 0.1J$) in our sLLG simulations. The Vampire simulations were conducted on a system comprising 24,000 spins, initiating from random spin configurations at high temperatures and progressively cooling to temperatures approaching $0\ K$. Multiple simulations with gradually increasing magnetic field strengths revealed the formation of Néel-type skyrmions within the magnetic field range of $0.12\ T \lesssim B \lesssim 0.225\ T$. However, due to the random nucleation of DMI-induced skyrmions[25–28], achieving perfectly ordered skyrmion lattices proved challenging. Therefore, we employed suitable functions to model the skyrmion lattice precisely, after determining the unit cell size from the Vampire simulations (refer to Supplementary Note 1 for details on our approach).

The real-space magnon Hamiltonian can be derived from Equation 1 by employing standard rotation techniques[7–9,29]. Specifically, Rodrigues' rotation formula is utilized to define a rotated frame, aligning its z-axis with the local spin direction within the skyrmionic ground state. Therefore, the classical ground state manifests as a ferromagnetic configuration in the rotated frame. This allows for the representation of rotated spin operators in terms of magnon creation (a_i^+) and annihilation (a_i) operators through the Holstein-Primakoff transformation[30]. By incorporating the rotated spin operators and their Holstein-Primakoff representations into Equation 1 (the detailed derivation is provided in Supplementary Notes 2 and 3), we determine the real-space magnon Hamiltonian as follows,

$$\mathcal{H} = \mathcal{H}^{ex} + \mathcal{H}^D + \mathcal{H}^{Zee}$$

(2a)

with,

$$\mathcal{H}^{ex} = JS \sum_{i,j,m} \left[\frac{1}{2} R_{mz,i}\, R_{mz,j}\, a_i^+ a_i - R_{m-,i}\, R_{m+,j}\, a_i^+\, a_j - R_{m-,i}\, R_{m-,j}\, a_i^+\, a_j^+ \right] + h.c.$$

(2b)

$$\mathcal{H}^D = S \sum_{i,j} \sum_{m,m_1,m_2} \in_{mm_1m_2} D_j^m \left[\frac{1}{2} R_{m_1z,i} R_{m_2z,j} a_i^+ a_i - R_{m_1-,i} R_{m_2+,j} a_i^+ a_j \right.$$

$$\left. - R_{m_1-,i} R_{m_2-,j} a_i^+ a_j^+ \right] + h.c.$$

$$(2c)$$

$$\mathcal{H}^{Zee} = BS \sum_i R_{zz,i} a_i^+ a_i + h.c.$$

$$(2d)$$

In Equation 2, the Hamiltonians $\mathcal{H}^{ex}$, $\mathcal{H}^D$, and $\mathcal{H}^{Zee}$ account for the exchange, DMI, and Zeeman contributions, respectively. The term 'h.c.' denotes Hermitian conjugation. The indices m, m_1, and m_2 are summed over x, y, and z. D_j^m and $\in_{mm_1m_2}$ stand for the components of the DMI vectors and the Levi-Civita symbol, respectively.

We aim to transform $\mathcal{H}$ from the real space to the Fourier (or momentum) space, thereby removing its dependency on the real space sites (i and j in Equation 2). This transition entails Fourier expansions of the rotation matrix elements R_{mn}, utilizing characteristic wave vectors defined by the skyrmion lattice. The optimal set of skyrmion wave vectors is derived from the Fourier expansion of the classical spin vectors that form the skyrmion lattice ground state.

As depicted in Figure 1b, the skyrmions form a triangular Bravais lattice with large real-space lattice vectors $\boldsymbol{a}_1$ and $\boldsymbol{a}_2$, and a correspondingly tiny Brillouin Zone (BZ), defined by reciprocal lattice vectors $\boldsymbol{b}_1$ and $\boldsymbol{b}_2$. The classical spin vector varies over a length scale much larger than the lattice spacings a, necessitating a continuum approach. In this approach, the classical ground state is represented as a continuous vector field $\boldsymbol{S}(\boldsymbol{r})$, which admits a Fourier series expansion in the form

$$\boldsymbol{S}(\boldsymbol{r}) = \sum_{\gamma,\sigma \in h} \left[\boldsymbol{S}^{\gamma\sigma} e^{i\mathbf{G}_{\gamma,\sigma}.\boldsymbol{r}} + \boldsymbol{S}^{\gamma\sigma*} e^{-i\mathbf{G}_{\gamma,\sigma}.\boldsymbol{r}} \right]$$

$$(3)$$

Here, $\mathbf{G}_{\gamma,\sigma} = \gamma \boldsymbol{b}_1 + \sigma \boldsymbol{b}_2$ (γ and σ are integers) represent the skyrmion wave vectors. The functional form of the continuous field $\boldsymbol{S}(\boldsymbol{r})$ is presented in Supplementary Note 1. The vector coefficients $\boldsymbol{S}^{\gamma\sigma}$ are calculated using the Fourier transform formula, $\frac{1}{A} \iint d^2r\, \boldsymbol{S}(\boldsymbol{r}) e^{\pm i\mathbf{G}_{\gamma,\sigma}.\boldsymbol{r}}$, performed numerically over the unit cell (a single skyrmion) with area A.

Our numerical analysis demonstrates that the Fourier series in Equation 3 yields excellent convergence with 64 wave vectors $\mathbf{G}_{\gamma,\sigma}$, compiled in the set $h = \{(0,\sigma) \mid 0 \leq \sigma \leq 6\} \cup \{(\gamma,\sigma) \mid 1 \leq \gamma \leq 6 \text{ and } \gamma - 6 \leq \sigma \leq 6\}$. The vectors $\boldsymbol{S}^{\gamma\sigma}$ can be expressed as $\boldsymbol{S}^{\gamma\sigma} = \langle i\mathcal{S}_x^{\gamma\sigma}, i\mathcal{S}_y^{\gamma\sigma}, \mathcal{S}_z^{\gamma\sigma} \rangle$, outlining a momentum-space spin texture (Figure 1c) comprising spins $\langle \pm \mathcal{S}_x^{\gamma\sigma}, \pm \mathcal{S}_y^{\gamma\sigma}, \mathcal{S}_z^{\gamma\sigma} \rangle$ located at sites $\pm \mathbf{G}_{\gamma,\sigma}$, respectively. As expected, the magnitudes of the momentum-space spins $\boldsymbol{S}^{\gamma\sigma}$ diminish significantly beyond the second BZ, as demonstrated in Figure 1d. This behavior is crucial for ensuring the convergence of the Fourier series expansion in Equation 3.
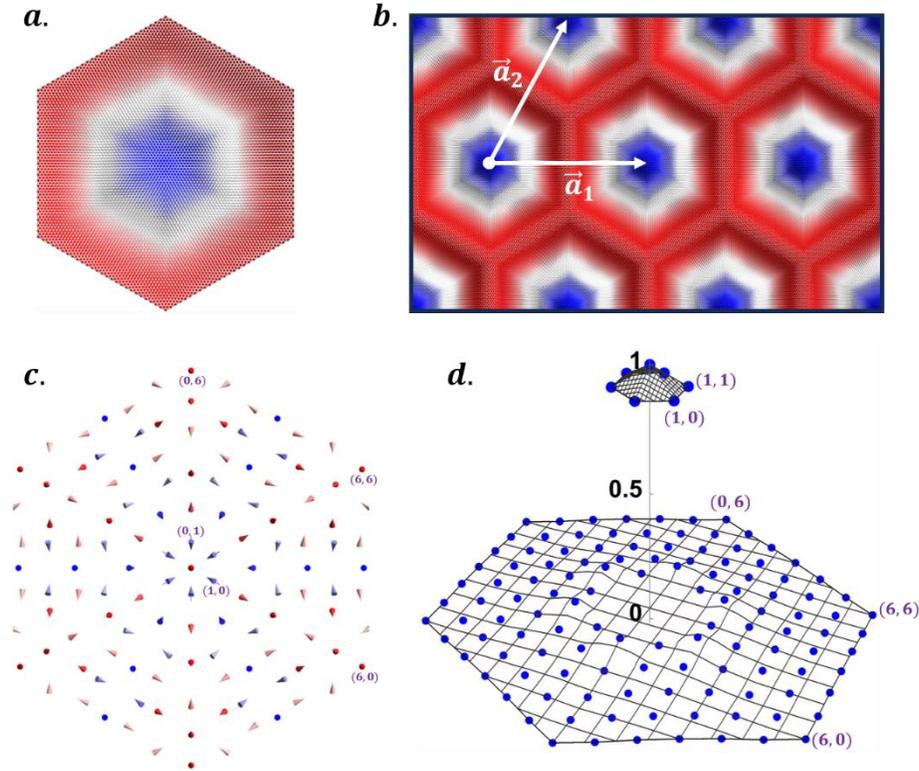
Figure 1. (a) A single Néel-type skyrmion with a DMI strength of $D = 0.1J$ and a magnetic field of $B = 0.12\,T$, encompassing 6163 spins. (b) The skyrmion lattice under these parameters, with $\boldsymbol{a}_1$ and $\boldsymbol{a}_2$ representing the real-space lattice vectors. (c) The momentum-space representation of the skyrmion lattice, with momentum-space spins located at positions (γ, σ), defined by the skyrmion wave vectors $\mathbf{G}_{\gamma,\sigma} = \gamma \boldsymbol{b}_1 + \sigma \boldsymbol{b}_2$, where $\boldsymbol{b}_1$ and $\boldsymbol{b}_2$ are the reciprocal-space lattice vectors. (d) The magnitudes of the momentum-space spins normalized with respect to the spin at the BZ center.

Next, we utilize Rodrigues' rotation formula to express the rotation matrix elements R_{mn} in terms of the components of the continuous field $\boldsymbol{S}(\boldsymbol{r})$, as detailed in Supplementary Note 2.

Consequently, these elements are defined as continuous functions $R_{mn}(\boldsymbol{r})$ and are expanded into Fourier series using the same set h of skyrmion wave vectors,

$$R_{mn}(\boldsymbol{r}) = \sum_{\gamma,\sigma\epsilon h}\left[\bar{Q}_{mn}^{\gamma\sigma}e^{i\boldsymbol{G}_{\gamma,\sigma}.\boldsymbol{r}} + Q_{mn}^{\gamma\sigma}e^{-i\boldsymbol{G}_{\gamma,\sigma}.\boldsymbol{r}}\right]$$

(4)

The Fourier coefficients $Q_{mn}^{\gamma\sigma}$ and $\bar{Q}_{mn}^{\gamma\sigma}$, with $m \in \{x, y, z\}$ and $n \in \{+, -, z\}$, are computed numerically using the Fourier transform formula $\frac{1}{A}\iint d^2r\, R_{mn}(\boldsymbol{r})e^{\pm i\boldsymbol{G}_{\gamma,\sigma}.\boldsymbol{r}}$.

In turn, the magnon operators are represented in the standard Fourier form, $a_i^+ = \frac{1}{\sqrt{N}}\sum_{\boldsymbol{k}} e^{-i\boldsymbol{k}.\boldsymbol{r}_i}a_{\boldsymbol{k}}^+$, where N represents the total number of lattice sites and $\boldsymbol{k}$ is a momentum within the first BZ. By substituting the Fourier expansions of $R_{mn}(\boldsymbol{r})$ and the magnon operators into $\mathcal{H}$ (Equation 2) and executing the summations over the real-space lattice sites, we successfully derive the magnon Hamiltonian in momentum space, as detailed in Supplementary Note 4. In the process, $\boldsymbol{k}$ from the first BZ couples with the skyrmion lattice wave vectors $\boldsymbol{G}_{\gamma,\sigma}$, introducing multi-momentum bosonic operators ($a_{\boldsymbol{k}\pm\boldsymbol{G}_{\gamma,\sigma}}^+$ and $a_{\boldsymbol{k}\pm\boldsymbol{G}_{\gamma,\sigma}}$) into the magnon Hamiltonian. The emergence of such operators in the Hamiltonian is a manifestation of the umklapp scattering processes experienced by magnons while traveling the skyrmion lattice.

The resulting momentum-space Hamiltonian can be written in compact form as follows,

$$\mathcal{H} = \frac{1}{2}\sum_{\boldsymbol{k}}\sum_{\gamma,\sigma\epsilon h}\left[\chi_{\gamma,\sigma;I}a_{\boldsymbol{k}}^+a_{\boldsymbol{k}+\boldsymbol{G}_{\gamma,\sigma}} + \tilde{\chi}_{\gamma,\sigma;I}a_{-\boldsymbol{k}}^+a_{-\boldsymbol{k}-\boldsymbol{G}_{\gamma,\sigma}} + \chi_{\gamma,\sigma;II}a_{\boldsymbol{k}}^+a_{-\boldsymbol{k}-\boldsymbol{G}_{\gamma,\sigma}}^+ + \tilde{\chi}_{\gamma,\sigma;II}a_{\boldsymbol{k}+\boldsymbol{G}_{\gamma,\sigma}}^+a_{-\boldsymbol{k}}^+\right]$$
$$+ h.c.$$

(5)

The coefficients $\chi_{\gamma,\sigma;I}$, $\tilde{\chi}_{\gamma,\sigma;I}$, $\chi_{\gamma,\sigma;II}$, and $\tilde{\chi}_{\gamma,\sigma;II}$ are complex functions of $\boldsymbol{k}$ and $\boldsymbol{G}_{\gamma,\sigma}$. For conciseness, the detailed derivation and the explicit expressions of these coefficients are provided in Supplementary Note 4.

To further explore the structure of $\mathcal{H}$ and its physical implications, we introduce the operator wave function $\Psi_{\boldsymbol{k}}^\dagger = [\phi_{\boldsymbol{k}}^\dagger \quad \phi_{-\boldsymbol{k}}^\dagger]$, with $\phi_{\boldsymbol{k}}^\dagger = \left[a_{\boldsymbol{k}+\boldsymbol{G}_{\gamma_1,\sigma_1}}^+ \quad \cdots \quad a_{\boldsymbol{k}+\boldsymbol{G}_{\gamma_n,\sigma_n}}^+ \quad a_{\boldsymbol{k}-\boldsymbol{G}_{\gamma_2,\sigma_2}}^+ \quad \cdots \quad a_{\boldsymbol{k}-\boldsymbol{G}_{\gamma_n,\sigma_n}}^+\right]$, and $\phi_{-\boldsymbol{k}}^\dagger = \left[a_{-\boldsymbol{k}-\boldsymbol{G}_{\gamma_1,\sigma_1}}^+ \quad \cdots \quad a_{-\boldsymbol{k}-\boldsymbol{G}_{\gamma_n,\sigma_n}}^+ \quad a_{-\boldsymbol{k}+\boldsymbol{G}_{\gamma_2,\sigma_2}}^+ \quad \cdots \quad a_{-\boldsymbol{k}+\boldsymbol{G}_{\gamma_n,\sigma_n}}^+\right]$. This allows Equation 5 to be recast in a matrix form as,

$$\mathcal{H} = \frac{1}{2} \sum_{k} \Psi_k^\dagger \mathcal{H}(\boldsymbol{k}, \boldsymbol{G}_{\gamma,\sigma}) \Psi_k$$

<div align="right">(6)</div>

with $\mathcal{H}(\boldsymbol{k}, \boldsymbol{G}_{\gamma,\sigma}) = \begin{bmatrix} H(\boldsymbol{k}, \boldsymbol{G}_{\gamma,\sigma}) & \Delta(\boldsymbol{k}, \boldsymbol{G}_{\gamma,\sigma}) \\ \Delta^\dagger(\boldsymbol{k}, \boldsymbol{G}_{\gamma,\sigma}) & \widetilde{H}(\boldsymbol{k}, \boldsymbol{G}_{\gamma,\sigma}) \end{bmatrix}$.

The block matrices within $\mathcal{H}(\boldsymbol{k}, \boldsymbol{G}_{\gamma,\sigma})$ are of dimensions $n \times n$, where $n = 64$ represents the number of relevant sites in momentum space, as specified by the set h. These blocks elucidate the permitted magnon umklapp scatterings in momentum space. For instance, an umklapp scattering event from $\boldsymbol{k} + \boldsymbol{G}_{\gamma_i,\sigma_i}$ to $\boldsymbol{k} + \boldsymbol{G}_{\gamma_j,\sigma_j}$ occurs if and only if there exists a pair $(\gamma_l, \sigma_l) \in h$ such that $(\gamma_i, \sigma_i) + (\gamma_l, \sigma_l) = (\gamma_j, \sigma_j)$. Such scattering generates the matrix elements $H_{ij} = \chi_{\gamma_l,\sigma_l;I}(\boldsymbol{k} + \boldsymbol{G}_{\gamma_i,\sigma_i})$, $\Delta_{ij} = \chi_{\gamma_l,\sigma_l;II}(\boldsymbol{k} + \boldsymbol{G}_{\gamma_i,\sigma_i})$, $\Delta_{ji} = \tilde{\chi}_{\gamma_l,\sigma_l;II}(\boldsymbol{k} + \boldsymbol{G}_{\gamma_i,\sigma_i})$, and $\widetilde{H}_{ji} = \tilde{\chi}_{\gamma_l,\sigma_l;I}(\boldsymbol{k} + \boldsymbol{G}_{\gamma_i,\sigma_i})$. Conversely, the reverse umklapp scattering, $(\gamma_j, \sigma_j) - (\gamma_l, \sigma_l) = (\gamma_i, \sigma_i)$, leads to the Hermitian conjugate matrix elements. By systematically accounting for all allowed umklapp scattering processes, we construct the matrix $\mathcal{H}(\boldsymbol{k}, \boldsymbol{G}_{\gamma,\sigma})$, which is inherently Hermitian. To determine the magnonic band structure, we apply the standard Bogoliubov transformation to diagonalize $\mathcal{H}(\boldsymbol{k}, \boldsymbol{G}_{\gamma,\sigma})$, utilizing the numerical approach developed by Colpa[31].

Skyrmionic magnon bands

For the DMI strength $D = 0.1\,J$ chosen in our study, the minimum magnetic field required to stabilize skyrmions is approximately $0.12\,T$, as determined through the sLLG simulations described in the previous section. The skyrmion reaches its maximum size under this minimal magnetic field, comprising 6163 spins (Figures 1a, b). Due to their Bosonic nature, magnons tend to accumulate in the low-energy bands, which are therefore the primary focus of our calculations. Figure 2a displays the lowest 15 magnonic bands of this skyrmion ground state, calculated along the symmetry axes depicted in Figure 2b. Henceforth, we label these bands sequentially from $n = 1$ to $n = 15$, in order of increasing energy.

Given the large size of the skyrmions and the correspondingly tiny BZ, the 15-band magnon spectrum is confined to low energies, not exceeding $0.2J$ (Figure 2a). The lowest-energy band ($n = 1$) remains nonzero at the Γ point (the BZ's center), indicating the absence of Goldstone modes. We observe a global bandgap of approximately $0.016J$ between the first and second bands, with the latter appearing notably flat compared to all other bands. Despite its apparent flatness, a 3D plot of this band reveals its dispersion within a narrow bandwidth, as depicted in Figure 2c. The second and third modes are separated by a sizeable global bandgap ($\sim 0.05J$), while a smaller

gap of about $0.017J$ separates the fourth and fifth modes. The low-energy bands $n = 1, \ldots, 4$ stand out as relatively isolated from the remaining bands, while the magnon spectrum becomes more compact beyond these bands. At higher energies, the bands exhibit several avoided crossing points where they approach each other at specific points in the BZ without actually closing the gaps. This phenomenon leads to the formation of numerous small bandgaps, examples of which are depicted in Figures 2d and 2e.
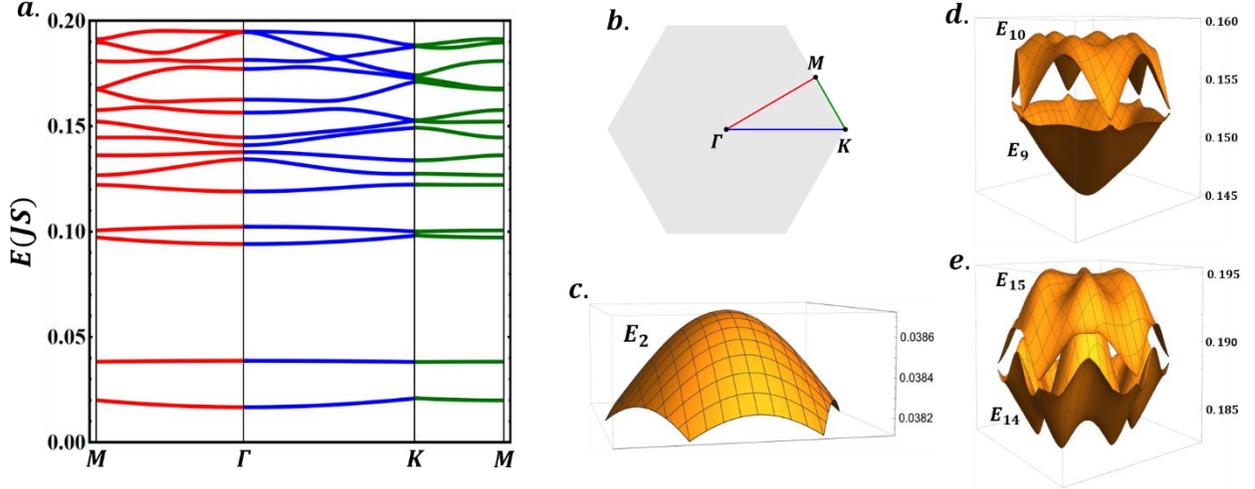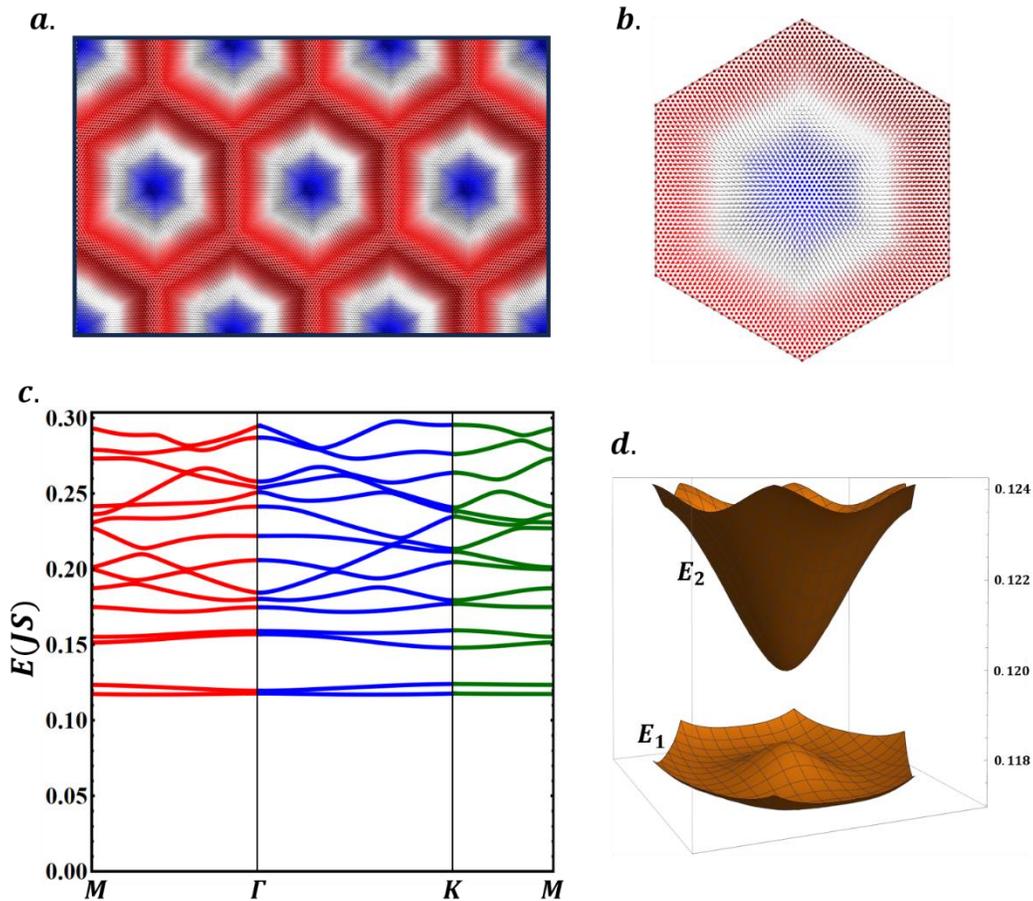

Figure 2. (a) Dispersion curves for the lowest 15 magnon bands of the skyrmion ground state at $D = 0.1J$ and $B = 0.12\ T$. The bands are plotted along the high-symmetry axes of the BZ shown in (b). (c) A 3D plot over the BZ of E_2 (the second energy band), revealing its dispersion within a narrow bandwidth. (d) A 3D plot over the BZ showing the tiny gaps between bands E_9 and E_{10}. (e) A similar plot to (d), but for bands E_{14} and E_{15}.

The gaped magnonic spectrum motivates the analysis of its topological features. Using the numerical method developed by Fukui *et al.*[32], we calculated the bands' Berry curvatures and Chern numbers. Details on the application of this numerical approach to multi-band spectra can be found elsewhere[33–35]. Our results for the Chern numbers (C_n, $n = 1, \ldots, 15$) are summarized in Table 1, and the Berry curvatures for the topological bands are presented in Figure S3 of Supplementary Note 5. For modes at higher energies, the tiny bandgaps lead to pronounced peaks in the Berry curvatures (Figure S3), which give rise to topological bands with various Chern numbers (Table 1). However, under the minimal magnetic field, the ground state may not be optimal for observing topological effects, as the lowest-energy bands are found to be topologically trivial (Table 1).

In our theory, the Hamiltonian $\mathcal{H}\left(\boldsymbol{k}, \boldsymbol{G}_{\gamma,\sigma}\right)$ is critically dependent on the reciprocal lattice vectors $\boldsymbol{b}_1$ and $\boldsymbol{b}_2$, which are determined by the size of the skyrmion. Thus, within the magnetic field range that stabilizes the skyrmion lattice, $0.12\ T \lesssim B \lesssim 0.225\ T$ at $D = 0.1\ J$, an increase in the magnetic field results in a reduction of the skyrmion size, which significantly impacts the

magnonic band structure. Specifically, at $B = 0.175\,T$, near the middle of the magnetic field range, the skyrmion size diminishes to 3661 spins, as illustrated in Figures 3a and 3b. The associated magnon band structure, shown in Figure 3c, differs markedly from that at the minimum magnetic field. The spectrum becomes more compact, reaching higher energies ($\sim 0.3\,J$) because of the larger reciprocal lattice vectors $\boldsymbol{b}_1$ and $\boldsymbol{b}_2$. Furthermore, the shift of the lowest energy mode to higher energies demonstrates the impact of skyrmion size—and, consequently, the magnetic field—on the energy gap of this mode. Although the lowest-energy band appears flat, closer examination shows that it is dispersive within a narrow range (Figure 3d). The four lowest-energy bands remain separated from the rest, while the spectrum's high-energy region is notably compact, featuring numerous tiny bandgaps at points of avoided crossing.

Figure 3. The skyrmion lattice (a) and a single skyrmion (b) obtained for a DMI strength of $D = 0.1J$ and a magnetic field of $B = 0.175\,T$. Each skyrmion comprises 3661 spins in this case. Figure (c) shows the dispersion curves for the lowest 15 magnon bands corresponding to the skyrmion lattice in (a). (d) A 3D plot over the BZ showing the first (E_1) and the second (E_2) energy bands, highlighting the narrow bandwidth dispersion of the first energy band and the gap between E_1 and E_2.

The size of the skyrmion, which correlates with the strength of the magnetic field, not only influences the profile of the magnon band structure but also significantly modifies its topology. Contrary to the minimal magnetic field case, at $B = 0.175\,T$, the entire band structure becomes topological, except for the two lowest energy bands (Table 1). The Berry curvatures for the topological bands at $B = 0.175\,T$ are depicted in Figure S4 of Supplementary Note 5. Notably, in the 15-band spectrum at $B = 0.175\,T$, the (relatively) high-energy bands ($n \geq 5$) are topological and densely packed, approaching the profile of a topological band continuum.

	C_1	C_2	C_3	C_4	C_5	C_6	C_7	C_8	C_9	C_{10}	C_{11}	C_{12}	C_{13}	C_{14}	C_{15}
$0.12\,T$	0	0	0	0	1	0	0	-1	0	0	5	-5	5	-2	2
$0.175\,T$	0	0	-1	2	2	1	3	-5	6	-5	6	-4	-1	-1	-3
$0.225\,T$	1	-1	3	1	-1	2	2	1	1	3	-1	1	-6	8	-4

Table 1. Chern numbers (C_n) for the lowest 15 magnon bands ($n = 1$ to $n = 15$, in order of increasing energy) at different magnetic fields: $0.12\,T$ (second row), $0.175\,T$ (third row), and $0.225\,T$ (fourth row).

Our findings thus far have shown a profound dependence of the magnon band structure and its topology on the magnetic field (or skyrmion size). To further explore this dependence, we consider next the maximal magnetic field value of $0.225\,T$. At this magnetic field, the skyrmion is formed of 2755 spins (Figure 4a, b). The 15-band spectrum for this case is presented in Figure 4c, showcasing a significantly different profile compared to the previous magnetic fields. The entire band structure shifts to higher energies, increasing the band gap for the lowest energy mode, while the highest energy band reaches a value near $0.38\,J$. All bands are dispersive at the maximal magnetic field, showing that flat bands are not a universal feature of the skyrmionic magnon band structure. The entire low-energy band structure becomes densely packed, resembling a band continuum (Figure 4c). More importantly, the calculation of the Berry curvature and Chern numbers reveals that all bands are topological (Table 1), with some Chern numbers reaching significant magnitudes (e.g., $C_{13} = -6$ and $C_{14} = 8$). The Berry curvatures for all 15 bands are illustrated in Figure S5 of Supplementary Note 5.

Finally, we have calculated the contributions of the 15 lowest energy bands to the density of states, which are depicted in Figures 4d-f for the magnetic fields of 0.125 T, 0.175 T, and 0.225 T, respectively. It is observed that higher magnetic fields promote the merging of peaks in the density of states due to the compaction effect previously discussed. However, the overall density of states decreases at higher magnetic fields (see Figure S6 of Supplementary Note 5), primarily due to the reduction in skyrmion size and the consequent increase in the BZ area.
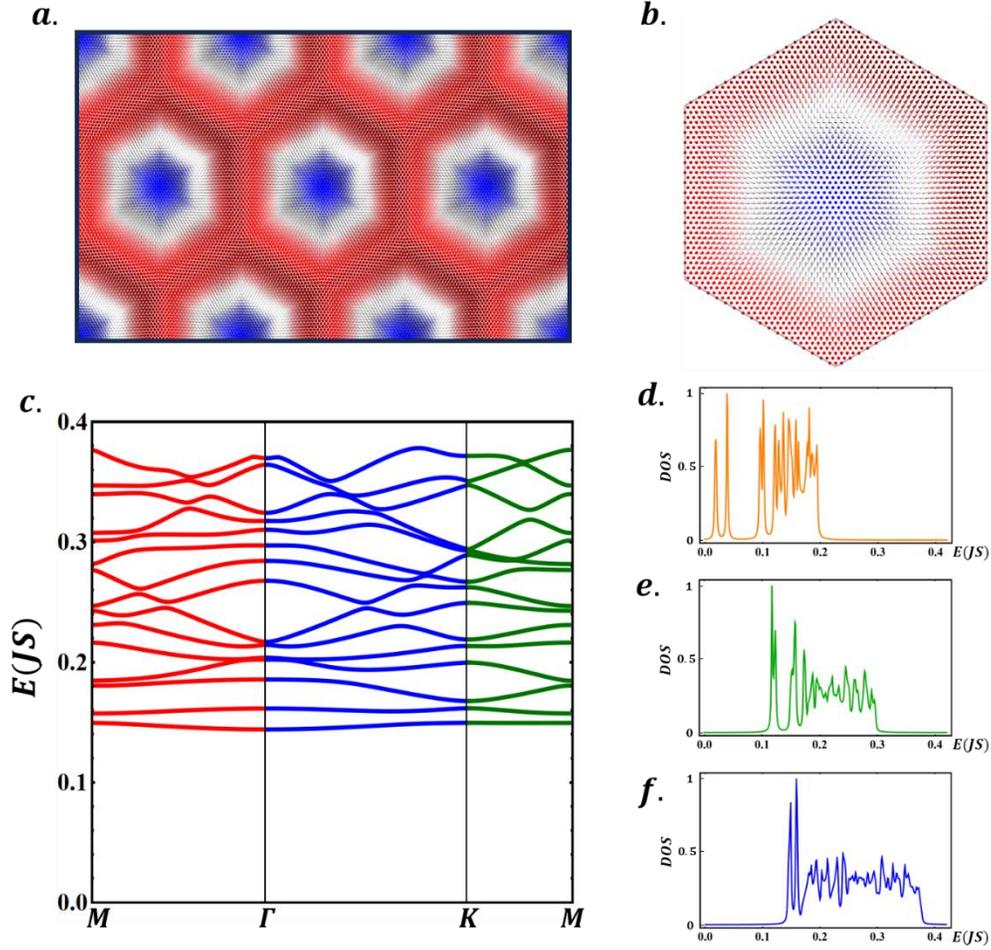
Figure 4. The skyrmion lattice (a) and a single skyrmion with 2755 spins (b) obtained for a DMI strength of $D = 0.1J$ and a magnetic field of $B = 0.225\ T$. (c) The dispersion curves for the lowest 15 magnon bands corresponding to the skyrmion lattice in (a). (d)-(f) Contributions of the 15 lowest energy bands to the density of states (DOS) for magnetic fields of 0.125 T, 0.175 T, and 0.225 T, respectively. In these plots, the DOS is normalized with respect to its maximum value.

Conclusion

We developed a momentum-space theory to describe magnon dynamics in large 2D ferromagnetic skyrmions as an alternative to the cluster approach. Using Fourier-space techniques and a continuum treatment of the skyrmions, we derived the magnon Hamiltonian exclusively in terms of momentum-space operators. In this picture, umklapp scattering of magnons becomes inevitable, leading to a multi-momentum Hamiltonian. The profile and topology of the low-energy magnon spectrum obtained from our Hamiltonian depend crucially on the magnetic field (hence the skyrmion's size), which can render the entire spectrum topological. Further, we found that flat bands are not universal features of the magnonic spectrum. Specifically, we observed a single

relatively flat band at low and moderate magnetic fields, which disappeared at a higher magnetic field.

The lowest-energy band is gapped near the BZ's center, indicating the absence of the Goldstone mode for the studied skyrmions. Nevertheless, the inverse relationship observed between the lowest-energy gap and the skyrmion size suggests that this mode could potentially be retrieved for extremely large skyrmions at very low DMI strengths. However, exploring this possibility at such extreme conditions is beyond the scope of this manuscript.

Our work specifically addresses 2D magnets without generalizing our conclusions to 3D magnets or magnetic thin films. Topological spin textures have been reported in several 2D magnets[36–48]. However, observing their magnons remains experimentally challenging, mainly due to the limitations of current measurement techniques and the difficulty in achieving sufficiently ordered skyrmion lattices[4,25–27,49]. Our focus on 2D magnets justifies the exclusion of dipolar interactions, which are generally considered weak in such materials[50–55].

The proposed theory awaits significant future developments. This includes an extension to other types of spin lattices, such as the honeycomb lattice, which characterizes several 2D magnets[48,56–58]. Additionally, it is crucial to integrate other fundamental interactions, such as intrinsic next-nearest-neighbor DMI (IDMI), Kitaev interactions, and magnetic anisotropies. Given that the IDMI and Kitaev interaction can induce 2D topological magnons even in a collinear ground state [50–55,59–63], examining their effects in skyrmion ground states offers an exciting avenue for further research. Furthermore, applying this theory to other topological spin textures[64], such as antiferromagnetic skyrmions, antiskyrmions, and bi-merons, would also be of considerable relevance.

Finally, we stress that the proposed theory is designed for large skyrmions, potentially with a lower size limit of several hundred spins per skyrmion. Meanwhile, the particular class of quantum skyrmions[17,65], which are smaller in size, indeed requires a cluster (or sublattice) approach to describe their magnon dynamics[12,13] accurately. Conversely, for the large skyrmions, the cluster approach becomes less practical and potentially less accurate, as it may obscure significant effects of the topological spin textures, which we sought to uncover in this study.

Acknowledgments

References

1. Van Hoogdalem, K. A., Tserkovnyak, Y. & Loss, D. Magnetic texture-induced thermal Hall effects. *Phys Rev B Condens Matter Mater Phys* **87**, 024402 (2013).

2. Petrova, O. & Tchernyshyov, O. Spin waves in a skyrmion crystal. *Phys Rev B Condens Matter Mater Phys* **84**, 214433 (2011).

3. Garst, M., Waizner, J. & Grundler, D. Collective spin excitations of helices and magnetic skyrmions: review and perspectives of magnonics in non-centrosymmetric magnets. *J Phys D Appl Phys* **50**, 293002 (2017).

4. Weber, T. *et al.* Topological magnon band structure of emergent Landau levels in a skyrmion lattice. *Science (1979)* **375**, 1025–1030 (2022).

5. Hirosawa, T., Mook, A., Klinovaja, J. & Loss, D. Magnetoelectric Cavity Magnonics in Skyrmion Crystals. *PRX Quantum* **3**, 040321 (2022).

6. Zhuo, F., Kang, J., Manchon, A. & Cheng, Z. Topological Phases in Magnonics. *Advanced Physics Research* 2300054 (2023) doi:10.1002/APXR.202300054.

7. Roldán-Molina, A., Nunez, A. S. & Fernández-Rossier, J. Topological spin waves in the atomic-scale magnetic skyrmion crystal. *New J Phys* **18**, 045015 (2016).

8. Díaz, S. A., Klinovaja, J. & Loss, D. Topological Magnons and Edge States in Antiferromagnetic Skyrmion Crystals. *Phys Rev Lett* **122**, 187203 (2019).

9. Diáz, S. A., Hirosawa, T., Klinovaja, J. & Loss, D. Chiral magnonic edge states in ferromagnetic skyrmion crystals controlled by magnetic fields. *Phys Rev Res* **2**, 013231 (2020).

10. Kim, S. K., Nakata, K., Loss, D. & Tserkovnyak, Y. Tunable Magnonic Thermal Hall Effect in Skyrmion Crystal Phases of Ferrimagnets. *Phys Rev Lett* **122**, 057204 (2019).

11. Akazawa, M. *et al.* Topological thermal Hall effect of magnons in magnetic skyrmion lattice. *Phys Rev Res* **4**, 043085 (2022).

12. Mæland, K. & Sudbø, A. Quantum fluctuations in the order parameter of quantum skyrmion crystals. *Phys Rev B* **105**, 224416 (2022).

13. Mæland, K. & Sudbø, A. Quantum topological phase transitions in skyrmion crystals. *Phys Rev Res* **4**, L032025 (2022).

14. Dos Santos, F. J., Dos Santos Dias, M., Guimarães, F. S. M., Bouaziz, J. & Lounis, S. Spin-resolved inelastic electron scattering by spin waves in noncollinear magnets. *Phys Rev B* **97**, 024431 (2018).

15. Dzyaloshinsky, I. A thermodynamic theory of 'weak' ferromagnetism of antiferromagnetics. *Journal of Physics and Chemistry of Solids* **4**, 241–255 (1958).

16. Moriya, T. Anisotropic superexchange interaction and weak ferromagnetism. *Physical Review* **120**, 91–98 (1960).

17. Heinze, S. *et al.* Spontaneous atomic-scale magnetic skyrmion lattice in two dimensions. *Nature Physics 2011 7:9* **7**, 713–718 (2011).

18. Finocchio, G., Büttner, F., Tomasello, R., Carpentieri, M. & Kläui, M. Magnetic skyrmions: from fundamental to applications. *J Phys D Appl Phys* **49**, 423001 (2016).

19. Mühlbauer, S. *et al.* Skyrmion lattice in a chiral magnet. *Science (1979)* **323**, 915–919 (2009).

20. Bauer, A., Garst, M. & Pfleiderer, C. Specific Heat of the Skyrmion Lattice Phase and Field-Induced Tricritical Point in MnSi. *Phys Rev Lett* **110**, 177207 (2013).

21. Buhrandt, S. & Fritz, L. Skyrmion lattice phase in three-dimensional chiral magnets from Monte Carlo simulations. *Phys Rev B Condens Matter Mater Phys* **88**, 195137 (2013).

22. Bauer, A. *et al.* Quantum phase transitions in single-crystal Mn1-xFe xSi and Mn1-xCoxSi: Crystal growth, magnetization, ac susceptibility, and specific heat. *Phys Rev B Condens Matter Mater Phys* **82**, 064404 (2010).

23. Schwarze, T. *et al.* Universal helimagnon and skyrmion excitations in metallic, semiconducting and insulating chiral magnets. *Nature Materials 2014 14:5* **14**, 478–483 (2015).

24. Evans, R. F. L. *et al.* Atomistic spin model simulations of magnetic nanomaterials. *Journal of Physics: Condensed Matter* **26**, 103202 (2014).

25. Ma, M., Pan, Z. & Ma, F. Artificial skyrmion in magnetic multilayers. *J Appl Phys* **132**, 043906 (2022).

26. Li, W. *et al.* Anatomy of Skyrmionic Textures in Magnetic Multilayers. *Advanced Materials* **31**, 1807683 (2019).

27. Li, Y. *et al.* An Artificial Skyrmion Platform with Robust Tunability in Synthetic Antiferromagnetic Multilayers. *Adv Funct Mater* **30**, 1907140 (2020).

28. Jabakhanji, B. & Ghader, D. Designing Layered 2D Skyrmion Lattices in Moiré Magnetic Heterostructures. *Adv Mater Interfaces* **11**, 2300188 (2024).

29. Singh, V. & Majumdar, P. Spin rotation technique for non-collinear magnetic systems: application to the generalized Villain model. *Journal of Physics: Condensed Matter* **21**, 216001 (2009).

30. Holstein, T. & Primakoff, H. Field Dependence of the Intrinsic Domain Magnetization of a Ferromagnet. *Physical Review* **58**, 1098 (1940).

31. Colpa, J. H. P. Diagonalization of the quadratic boson hamiltonian. *Physica A: Statistical Mechanics and its Applications* **93**, 327–353 (1978).

32. Fukui, T., Hatsugai, Y. & Suzuki, H. Chern numbers in discretized Brillouin zone: Efficient method of computing (spin) Hall conductances. *J Physical Soc Japan* **74**, 1674–1677 (2005).

33. Zhang, Y. H., Mao, D., Cao, Y., Jarillo-Herrero, P. & Senthil, T. Nearly flat Chern bands in moiré superlattices. *Phys Rev B* **99**, 075127 (2019).

34. Ghader, D. Magnon magic angles and tunable Hall conductivity in 2D twisted ferromagnetic bilayers. *Sci Rep* **10**, 15069 (2020).

35. Li, Y. H. & Cheng, R. Moiré magnons in twisted bilayer magnets with collinear order. *Phys Rev B* **102**, 094404 (2020).

36.   Han, M.-G. *et al.* Topological Magnetic-Spin Textures in Two-Dimensional van der Waals Cr 2 Ge 2 Te 6. *Nano Lett* **19**, 7859–7865 (2019).

37.   Ding, B. *et al.* Observation of Magnetic Skyrmion Bubbles in a van der Waals Ferromagnet Fe 3 GeTe 2. *Nano Lett* **20**, 868–873 (2020).

38.   Yang, M. *et al.* Creation of skyrmions in van der Waals ferromagnet Fe 3 GeTe 2 on (Co/Pd) n superlattice. *Sci Adv* **6**, eabb5157 (2020).

39.   Wu, Y. *et al.* Néel-type skyrmion in WTe2/Fe3GeTe2 van der Waals heterostructure. *Nat Commun* **11**, 3860 (2020).

40.   Xu, C. *et al.* Topological spin texture in Janus monolayers of the chromium trihalides Cr(I, X)3. *Phys Rev B* **101**, 060404 (2020).

41.   Cui, Q., Liang, J., Shao, Z., Cui, P. & Yang, H. Strain-tunable ferromagnetism and chiral spin textures in two-dimensional Janus chromium dichalcogenides. *Phys Rev B* **102**, 094425 (2020).

42.   Yuan, J. *et al.* Intrinsic skyrmions in monolayer Janus magnets. *Phys Rev B* **101**, 094420 (2020).

43.   Sun, W. *et al.* Controlling bimerons as skyrmion analogues by ferroelectric polarization in 2D van der Waals multiferroic heterostructures. *Nat Commun* **11**, 5930 (2020).

44.   Xu, C. *et al.* Electric-Field Switching of Magnetic Topological Charge in Type-I Multiferroics. *Phys Rev Lett* **125**, 037203 (2020).

45.   Liang, J., Cui, Q. & Yang, H. Electrically switchable Rashba-type Dzyaloshinskii-Moriya interaction and skyrmion in two-dimensional magnetoelectric multiferroics. *Phys Rev B* **102**, 220409 (2020).

46.   Lu, X., Fei, R., Zhu, L. & Yang, L. Meron-like topological spin defects in monolayer CrCl3. *Nat Commun* **11**, 4724 (2020).

47.   Augustin, M., Jenkins, S., Evans, R. F. L., Novoselov, K. S. & Santos, E. J. G. Properties and dynamics of meron topological spin textures in the two-dimensional magnet CrCl3. *Nat Commun* **12**, 185 (2021).

48.   Wang, Q. H. *et al.* The Magnetic Genome of Two-Dimensional van der Waals Materials. *ACS Nano* Preprint at https://doi.org/10.1021/acsnano.1c09150 (2021).

49.   Soda, M. *et al.* Asymmetric slow dynamics of the skyrmion lattice in MnSi. *Nature Physics 2023 19:10* **19**, 1476–1481 (2023).

50.   Lee, I. *et al.* Fundamental Spin Interactions Underlying the Magnetic Anisotropy in the Kitaev Ferromagnet CrI3. *Phys Rev Lett* **124**, 017201 (2020).

51.   Cai, Z. *et al.* Topological magnon insulator spin excitations in the two-dimensional ferromagnet CrBr3. *Phys Rev B* **104**, L020402 (2021).

52.   Aguilera, E., Jaeschke-Ubiergo, R., Vidal-Silva, N., Torres, L. E. F. F. & Nunez, A. S. Topological magnonics in the two-dimensional van der Waals magnet CrI3. *Phys Rev B* **102**, 024409 (2020).

53.   Chen, L. *et al.* Magnetic anisotropy in ferromagnetic CrI3. *Phys Rev B* **101**, 134418 (2020).

54. Chen, L. *et al.* Topological Spin Excitations in Honeycomb Ferromagnet CrI3. *Phys Rev X* **8**, 041028 (2018).

55. Pershoguba, S. S. *et al.* Dirac Magnons in Honeycomb Ferromagnets. *Phys Rev X* **8**, 011010 (2018).

56. Huang, B. *et al.* Layer-dependent ferromagnetism in a van der Waals crystal down to the monolayer limit. *Nature* **546**, 270–273 (2017).

57. Gong, C. *et al.* Discovery of intrinsic ferromagnetism in two-dimensional van der Waals crystals. *Nature* **546**, 265–269 (2017).

58. Soriano, D., Katsnelson, M. I. & Fernández-Rossier, J. Magnetic Two-Dimensional Chromium Trihalides: A Theoretical Perspective. *Nano Lett* **20**, 6225–6234 (2020).

59. Owerre, S. A. A first theoretical realization of honeycomb topological magnon insulator. *Journal of Physics Condensed Matter* **28**, 386001 (2016).

60. Ghader, D. Insights on magnon topology and valley-polarization in 2D bilayer quantum magnets. *New J Phys* **23**, 053022 (2021).

61. Ghader, D. Theoretical realization of rich magnon topology by symmetry-breaking in honeycomb bilayer ferromagnets. *Physica E Low Dimens Syst Nanostruct* **135**, 114984 (2022).

62. Ghader, D., Gao, H., Radaelli, P. G., Continenza, A. & Stroppa, A. Theoretical Study of Magnon Spin Currents in Chromium Trihalide Hetero-bilayers: Implications for Magnonic and Spintronic Devices. *ACS Appl Nano Mater* **5**, 15150–15161 (2022).

63. Pires, A. S. T. Theoretical Tools for Spin Models in Magnetic Systems. *Theoretical Tools for Spin Models in Magnetic Systems* (2021) doi:10.1088/978-0-7503-3879-0.

64. Göbel, B., Mertig, I. & Tretiakov, O. A. Beyond skyrmions: Review and perspectives of alternative magnetic quasiparticles. *Phys Rep* **895**, 1–28 (2021).

65. Lohani, V., Hickey, C., Masell, J. & Rosch, A. Quantum Skyrmions in Frustrated Ferromagnets. *Phys Rev X* **91**, 041063 (2019).